Influence of build rate and post-AM surface treatments on fatigue life of powder bed fusion – laser beam 316L stainless steel

Citation for the original published paper (version of record):
Gunnerek, R., Kumarasinghe, S., Moverare, J. et al (2026). Influence of build rate and post-AM surface treatments on fatigue life of powder bed fusion –
laser beam 316L stainless steel. Journal of Materials Research and Technology, 42: 8979-8989.
http://dx.doi.org/10.1016/j.jmrt.2026.05.183

Journal of Materials Research and Technology 42 (2026) 8979–8989

Contents lists available at ScienceDirect

Journal of Materials Research and Technology

journal homepage: www.elsevier.com/locate/jmrt

Influence of build rate and post-AM surface treatments on fatigue life of powder bed fusion – laser beam 316L stainless steel

Rasmus Gunnerek [a,*], Subhani Buddhika Kumarasinghe [b], Johan Moverare [b], Tatiana Misuhrova [c,d], Uta Klement [a], Eduard Hryha [a]

[a] *Industrial and Materials Sciences, Chalmers University of Technology, SE- 412 96, Gothenburg, Sweden*
[b] *Division of Engineering Materials, Linköping University, SE-581 83, Linköping, Sweden*
[c] *Bundesanstalt für Materialforschung und -prüfung (BAM), Unter den Elchen 87, Berlin, 12205, Germany*
[d] *Helmoltz Zentrum Berlin, Hahn-Meitner-Platz 1, Berlin, 14109, Germany*

ARTICLE INFO

Keywords:
Productivity
Build rate
Powder bed fusion
Laser beam
Pore characteristics
Surface treatment
Additive manufacturing

ABSTRACT

This study investigates the influence of increased build rates on the high-cycle fatigue (HCF) life of PBF-LB manufactured 316L stainless steel by detailed analysis of pore characteristics using X-ray Computed Tomography (XCT) and surface roughness. Furthermore, the effects of post-processing surface treatments by chemical mechanical processing (CMP) and Hirtisation® on surface improvement and fatigue life were studied as well. Although increased build rates led to reduced fatigue life compared to the reference condition, this was related to distinct pore morphologies revealed by XCT. Specifically, the impact of porosity generated by increased hatch distance (PA) exhibited more uniform lack of fusion (LoF) pores, while porosity generated by higher scan speed (PB), displayed larger, more randomly distributed defects, leading to larger scatter in fatigue life. Examination of the fracture surfaces confirmed that crack initiation sites were associated with surface defects in the reference samples, LoF along the hatch lines in the PA samples, and larger, randomly distributed LoF pores in the PB samples. Both CMP and Hirtisation® surface treatments approximately doubled the fatigue life of the reference condition. However, limited material removal in CMP exposed subsurface porosity, acting as initiation sites. In contrast, the material removal during Hirtisation® effectively mitigated surface and near-surface defects. These findings highlight the critical role of build strategy in controlling defect morphology and the effectiveness of surface treatments in enhancing the fatigue performance of additively manufactured stainless steel, crucial for expanding their industrial applications.

1. Introduction

Powder bed fusion – laser beam (PBF-LB) technology offers a potential transformation in component manufacturing. It offers design freedom, material efficiency, and the ability to create complex, lightweight designs that can outperform components made by traditional formative or subtractive methods in terms of sustainability [1]. The 316L stainless steel is one of the most studied materials for PBF-LB. This is due to the good processability and the wide range of applications resulting from the excellent corrosion resistance and mechanical properties [2]. Compared to other as-built alloys processed by PBF-LB, such as nickel-based superalloys, other steels, and titanium-based alloys, 316L exhibits notable static properties, including high ductility (above 40%) and a yield strength exceeding 550 MPa [3], making it one of the more developed alloys for PBF-LB. However, inherent characteristics of the as-built condition, such as high surface roughness and internal defects, negatively impact the dynamic properties, especially the fatigue properties, which hinders wider industrial adoption [4].

Another bottleneck is the high cost of PBF-LB materials, largely due to low production volumes and slow process speeds [5]. Efforts to reduce build time have focused on increasing the number of lasers [6], using larger machines, and scaling the key printing parameters i.e. layer thickness, scan speed and hatch distance [7], [8], to reduce the build time of the process. Increasing the build rate often comes at the expense of part quality, which can lead to increased surface roughness and internal defects. Original equipment manufacturers (OEM)s of PBF-LB machines typically offers self-developed material licences that contain predefined process parameters. These licenses specify the expected

---

* Corresponding author.
E-mail address: rasmus.gunnerek@chalmers.se (R. Gunnerek).

https://doi.org/10.1016/j.jmrt.2026.05.183
Received 3 October 2025; Received in revised form 1 May 2026; Accepted 16 May 2026

quality in terms of density level, and the productivity is typically quantified by its build rate (see Eq. (1)). The build rate, a function of the main process parameter (layer thickness (t), scan speed (v) and hatch distance (hd)), provides an estimation of the volume of material produced per hour.

$$Build\ rate = v \cdot hd \cdot t \left(\frac{cm^3}{h}\right) \tag{1}$$

$$Volumetric\ energy\ density = \frac{p}{v \cdot hd \cdot t} = \frac{p}{Build\ rate} \left(\frac{J}{mm^3}\right) \tag{2}$$

Part quality, in terms of porosity level, typically correlates well with volumetric energy density (VED) (Eq. (2)), which describes the energy input per unit volume based on main printing parameters (layer thickness, scan speed, laser power (p) and hatch distance). To ensure proper interlayer formation and sufficient overlap of the melt pools to prevent porosity due to lack of fusion (LoF), sufficient VED is required. The sharp morphology of LoF pores, formed at low VED, can significantly reduce the structural integrity of PBF-LB parts [9]. In contrast, excessive VED can lead to keyhole porosity, which tends to be more spherical [10]. Examining the VED equation reveals that it can be expressed as the laser power divided by the build rate. Hence, increasing layer thickness, hatch distance or scan speed will decrease the VED. Compensating for this increased build rate requires higher laser power, however, common PBF-LB systems are often limited to around 500 W, which restricts the extent to which laser powder can be increased to accommodate larger build rates.

Studies have explored the static properties of PBF-LB 316L produced at increased build rates [11,12]. Leicht et al. found that increasing layer thickness from 20 to 80 μm (a 4x build time reduction) lowered yield strength from 540 to 465 MPa and elongation from 61% to 44, although still above wrought material standards. The major cause of the reduction in ductility was explained by the introduction of LoF pores when printing with higher layer thickness [11]. Choo et al. [12] showed that the orientation of the LoF pores relative to the load has a significant influence on the tensile properties. If the major axes of the pores were parallel to the load direction, minimal impact on static properties was observed even at larger porosity levels of 1.8%. Gong et al. [9] investigated the impact of defect type on static and fatigue properties of PBF-LB/Ti64 at different porosity levels (1% and 5% porosity). They showed that keyhole porosity up to 1% did not compromise the tensile properties, but the elongation was greatly affected at a porosity of 5%. Corresponding porosity levels containing LoF pores showed an even larger reduction in elongation and tensile strength. Thus, the static properties are reduced by increased build rates, but the properties can be controlled and adjusted by appropriate knowledge of the pore type and morphology at different process parameters.

Compared to the static properties, the fatigue behaviour of PBF-LB materials produced at high build rates are less explored. This is mainly due to the poor surface roughness (typical Ra values range from 3 to 30 μm) of as-built parts, which deteriorates further at higher build rates. Larger layer thickness can lead to increased roughness by sintered powder and the staircase effect on the surface [13]. These surface defects act as stress concentrations and serve as crack initiation sites, which are extremely sensitive to high cycle fatigue (HCF) life. Several methods aim to improve fatigue life by reducing roughness and including optimizing process parameters like contour scans. A contour scan of the outer surface, if optimized, can reduce powder adhesion, smoothen melt pool boundaries and limit dross formation [14]. However, as optimized process parameters can only reduce surface roughness to a certain degree, post-processing techniques like machining are often employed. This somewhat contradicts the near-net shape benefits of PBF-LB, as machining can be challenging for complex geometries and adds overall cost. Conversely, after machining of the surface, the effect of internal porosity determines the HCF of PBF-LB/316L. Andreau et al. [15] showed that a 25% increase in build rate had no effect on fatigue life when the surface was machined, even though internal pores with a size of up to 380 μm were present. It was further demonstrated that a thin contour significantly improves the fatigue life of porous PBF-LB/316L, with up to 10 % porosity not affecting fatigue properties. However, the study emphasised the need for new shape descriptors to better understand the fatigue behaviour and its connection to the complex morphology of PBF-LB generated pores at increased build rates. Given the established link between pore morphology and orientation at increased build rates and static properties, similar knowledge is required for fatigue.

This study aims to establish a relationship between build rate, pore morphology, surface roughness and the fatigue strength of PBF-LB/316L by analysing the influence of different types of pores at similar build rates in the as-built conditions. The study also investigates the influence of two post-processing treatments suitable for complex geometries, which contribute to the understanding of dynamic performance and expand the application areas of these materials.

2. Material and methods

2.1. Powder feedstock and sample manufacturing

Gas-atomized 316L stainless steel powder was supplied by EOS GmbH, Germany, with a particle size distribution of $d_{10} = 25$ μm, $d_{50} = 36$ μm, and $d_{90} = 54$ μm. The chemical composition is summarized in Table 1.

Cylindrical fatigue bars (90 mm height, 6 mm gauge diameter) were fabricated vertically using an EOS M290 machine, using an 80 μm layer thickness and a 67° rotation of the scan pattern between layers. A contour scanning strategy was applied with a laser power of 170 W and a scan speed of 400 mm/s, the complete set of process parameters is summarized in Table 2. The experimental matrix was designed to establish a high-density reference condition (~99.99% density), followed by incremental increases in build rate to introduce target porosity levels of approximately 1% and 5%, following the approach of Gong et al. [9]. For each increase in build rate, two distinct types of porosity were introduced: Porosity A (inter-hatch porosity), achieved by increasing the hatch spacing, and Porosity B (inter-layer porosity), achieved by increasing the scan speed, while keeping all other parameters constant relative to the reference condition. Notably, for each target porosity level, the VED and resulting build rate were identical for the corresponding Porosity A and Porosity B conditions. These conditions are denoted PA (Porosity A) and PB (Porosity B), with the numeric suffix 1 or 2 indicating the lower (~1%) or higher (~5%) porosity level, respectively (see Table 2).

2.2. Roughness measurements

The as-built fatigue bars were separated from the build plate using a band saw, and surface roughness measurements were subsequently conducted on selected samples. Surface characterization was performed using a SensoFar NeoxS optical profilometer operating in Confocal Fusion mode, equipped with a Nikon ×20 objective lens. Data acquisition and analysis were carried out using MountainsMap 10.1 software. For each condition listed in Table 2, three stitched surface regions (0.65×5.34 mm^2) were measured along the gauge section of one representative specimen. The reported mean values and standard deviations were calculated from these three measurements. Key surface texture parameters *Sa*, *S10z*, and *Sq* (μm) were selected in accordance with ISO 25178-2 [15] for comparative analysis.

Table 1
Powder chemical composition of 316L stainless steel in wt.%.

	C	Ni	Cr	Mo	Mn	Si	Fe
AISI 316L	0.018	13.4	17.1	2.73	1.42	0.38	Balance

Table 2

Process parameters for the high-density reference and porosity-induced conditions (PA1-2, PB1-2), including laser power (P), scan speed (v), hatch distance (hd), layer thickness (t), build rate (BR) and volumetric energy density (VED).

	Conditions	Level	p (W)	v (mm/s)	hd (µm)	t (µm)	BR (cm^3/h)	VED (J/mm^3)
Baseline 80 µm	Productivity high density	REF	280	800	100	80	23	43.8
Increased hatch distance	Porosity A Inter-hatch	PA1	280	800	**160**	80	37	27.3
		PA2	280	800	**190**	80	44	23
Increased scan speed	Porosity B Inter-layer	PB1	280	**1280**	100	80	37	27.3
		PB2	280	**1520**	100	80	44	23

2.3. *Post-AM surface treatments*

To investigate the effect of surface quality on fatigue performance, two distinct post-processing methods, chemical mechanical polishing (CMP) and Hirtisation®, were applied to the reference condition specimens (Table 2).

CMP was performed by REM Surface Engineering (Brenham, Texas, USA). The process combines controlled chemical surface modification with mechanical interaction using high-density ceramic media in a vibratory system. A proprietary compound formulated for 316L stainless steel promotes the formation of a thin, weakly bonded surface layer, which is subsequently removed through media interaction. This cyclic mechanism enables preferential smoothing of surface asperities without aggressive bulk abrasion. Under the applied conditions, approximately 110 µm of material was removed from the surface. A detailed description of the process chemistry, media characteristics, and surface interaction mechanisms for PBF-LB 316L has been reported previously [16].

In addition to CMP, the Hirtisation® process (RENA Technologies, Austria) is an alloy-specific electrochemical surface treatment [17] that combines chemical polishing with controlled anodic dissolution. The process selectively removes surface and near-surface material, preferentially acting on geometrical irregularities and surface-connected defects. In the present study, an average material removal depth of approximately 400 µm was achieved. The electrochemical setup and dissolution mechanisms for PBF-LB 316L have been described in previous work [18].

2.4. *Pore characteristics by X-ray computed tomography*

X-ray computed tomography (XCT) was performed on the fatigue bars using a GE v|tome|x 300 L laboratory CT scanner operated at 200 kV and 40 µA. The scans were restricted to the gauge region of each sample, with a reconstructed voxel size of 8 µm. To minimize false detection, pores smaller than 30 µm in diameter were excluded from the analysis.

Pore segmentation and preliminary analysis were conducted using Avizo software, with further quantitative processing carried out in MATLAB. Pore size was characterized by the equivalent diameter, while sphericity was used to assess the pore shape. Sphericity was calculated from the pore volume (V) and surface area (A) using Equation (3):

$$Sphericity = \frac{6 \times \pi^{0.5} \times V}{A^{1.5}} \tag{3}$$

Additionally, the orientation of each pore was evaluated relative to the build direction, defined as the angle between the pore principal axis and the vertical build axis. An orientation close to 90° indicates alignment parallel to the build direction. This analysis aimed to identify potential correlations between the processing parameters and any preferential pore orientation.

2.5. *Fatigue setup and fractography*

Fatigue tests were performed following ISO 1099:2018 [19] standard for axial force-controlled fatigue testing of metallic materials. The Instron WaveMatrix system, with a dynamic load capacity of ±50 kN and operated at a frequency of 5 Hz was used. Throughout the tests, a stress ratio ($R = \sigma_{min}/\sigma_{max}$) of -1 was applied. All the fatigue test series were performed with stress amplitudes between 100 MPa and 275 MPa, corresponding to stress ranges of 200 - 550 MPa. The applied forces were adjusted to be consistent with the reduced cross-sectional area due to post-treatments. S–N curves were plotted for all seven conditions following ASTM E739-10 [20].

All fractographic analyses were performed using a JEOL JSM-IT500 scanning electron microscope (SEM). The examination focused on the bottom half of the specimens, specifically selecting those samples that failed under fatigue testing at a stress range of 350 and 450 MPa.

3. Results and discussion

3.1. *Surface topography*

Fig. 1 presents 3D surface topography maps of the gauge sections for the as-built and surface-treated fatigue specimens, illustrating surface height variations along the build direction. All as-built conditions (Fig. 1a–b) exhibit the characteristic rough surface morphology of PBF-LB materials, with irregular peaks and valleys associated with adhered or partially sintered powder and melt pool overlap features formed during laser scanning [21]. Despite the changes in build rate and porosity generation strategy (PA vs PB), the overall appearance of the as-built surfaces is similar.

The roughness values summarized in Table 3 confirm these observations. The reference condition exhibited the lowest across all metrics, with a $Sa = 10.7 \pm 0.7$ µm. However, the differences between as-built surface conditions are small, and overlapping standard deviations indicate that the applied contour strategy produced comparable surface profiles regardless of whether the build rate was increased through hatch distance (PA) or scan speed (PB). The PB1 condition showed slightly higher values in ten-point height *S10z* (229.5 ± 80 µm), and largest variation. Since *S10z* is sensitive to extreme peaks or valleys, minor surface anomalies can exaggerate this value. The results indicate that increasing build rate had limited influence on the roughness in the as-built state.

The post-processed specimens (Fig. 1c) show a clear reduction in surface roughness. After CMP treatment a clear planarization of the surface is observed, resulting in reduced surface roughness relative to the as-built condition ($Sa = 5.7 \pm 2.0$ µm). However, semi-spherical valleys remain visible after treatment. The CMP process relies on mechanical interaction between the surface and high-density ceramic media, which mainly targets surface peaks [16]. With greater material removal, a further reduction in roughness would be expected. However, the applied removal depth (~110 µm) may have exposed subsurface porosity located in the transition region between the contour and bulk scan parameters. The opening of such features can limit further improvement of PBF-LB materials by surface treatment, as newly exposed defects may act as stress concentrators [22].

Hirtisation® resulted in the lowest surface roughness, with $Sa = 2.9 \pm 0.2$ µm. The 3D topography plots reveal reduced peak-to-valley height variations and a more uniform surface morphology compared to the as-built conditions. In agreement with previous work [18,23], the electrochemical treatment removes adhered and sintered powder particles

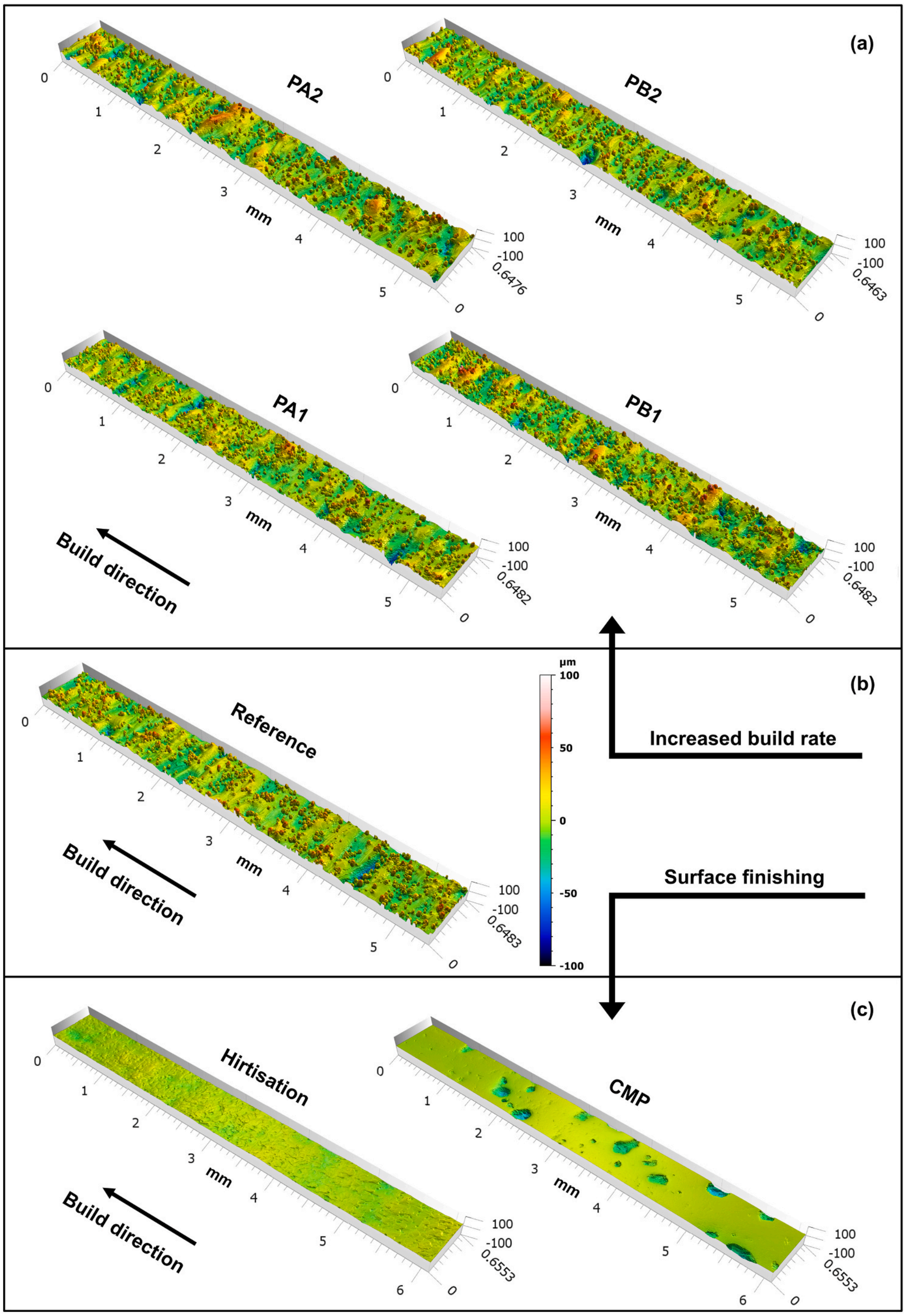

Fig. 1. 3D surface topography maps of the gauge sections for all investigated conditions: (a) as-built specimens produced at increasing build rates (PA1, PA2, PB1, PB2), (b) as-built high-density reference condition, and (c) reference specimens after surface treatments (Hirtisation® and CMP). The build direction (mm) is indicated in each panel. The colour bar represents height deviations in µm, ranging from −100 to +100 µm.

and preferentially dissolves material along melt pool boundaries. In contrast to CMP a greater material removal depth (~400 µm) was applied during Hirtisation®, effectively eliminating subsurface porosity in the contour-bulk transition region.

3.2. Pore characteristics by X-ray computed tomography

Fig. 2 illustrates cross-sectional (XY-plane) views of the pore distribution in the gauge sections, perpendicular to the build direction, for each condition. At the lowest build rate (23 cm^3/h), the reference condition exhibits a minimal pore fraction of 0.07%, with only a few small, spherical pores visible near the sample surface.

At a build rate of 37 cm^3/h, the pore fraction increases to 1.3% in PA1 and 0.7% in PB1. The PA1 condition shows a relatively uniform distribution of small, slightly elongated pores across the section, indicating that increased hatch spacing promotes consistent, controlled pore formation. In contrast, PB1 exhibits fewer but larger and more irregular pores, with a more scattered and less uniform distribution. Some defects appear clustered near the edges, suggesting that the increased scan speed may have reduced melt pool stability, resulting in incomplete fusion in localized areas.

At the highest build rate of 44 cm^3/h, the pore fraction further

Table 3
Surface roughness parameters (mean ± standard deviation) for each as-built and surface treated condition. Parameters include arithmetic mean height (*Sa*), ten-point height (*S10z*), and root mean square height (*Sq*), measured in accordance with ISO 25178-2.

Condition	*Sa* (μm)	*S10z* (μm)	*Sq* (μm)
Reference	10.7 ± 0.7	150 ± 20	14.4 ± 0.8
PA1	12.3 ± 0.4	160 ± 20	15.9 ± 0.3
PA2	11.0 ± 0.7	200 ± 40	14.7 ± 0.8
PB1	13.3 ± 0.7	230 ± 80	17 ± 1
PB2	12 ± 1	160 ± 40	15.7 ± 0.8
Hirtisation®	2.9 ± 0.2	25.8 ± 2	3.7 ± 0.2
CMP	5.7 ± 2.0	69.7 ± 20	9.8 ± 3.4

increases to 3.1% in PA2 and 3.6% in PB2. In PA2, pores remain relatively evenly distributed, though both size and number increase compared to PA1. However, the PB2 condition presents more severe pore characteristics. Large, irregular defects are distributed randomly throughout the section. Visible surface-connected pores are also present, seen near the outer boundary in the lower right region of the micrograph. These defects are critical from a fatigue perspective, as they can act as crack initiation sites [24].

Fig. 3 presents XCT reconstructions of pore distribution along the build direction (BD) for the different as-built conditions, complementing the cross-sectional (XY-plane) analysis shown in Fig. 2. The largest pores are extracted and highlighted in red for each condition. While the XY-plane views provide insight into surface proximity, a key factor influencing fatigue life [3], the BD plane reveals how pores are distributed vertically through the part.

The reference condition (lowest build rate) exhibits few, small, and nearly spherical pores, located approximately 100 μm from the surface, the largest of these is ~50 μm in diameter. As build rate increases, both the size and number of pores increase significantly. At intermediate build rates (PA1 and PB1), larger and more irregularly shaped pores appear, some of which extend both parallel and perpendicular to the build direction. At the highest build rates (PA2 and PB2), even larger, interconnected pore networks are observed. These structures indicate that higher build rates promote pore interconnectivity across multiple layers and in between hatches. Visual inspection also suggests a difference in pore orientation between PA and PB conditions. In PB2, pores appear more frequently oriented perpendicular to the build direction, reflecting inter-layer LoF.

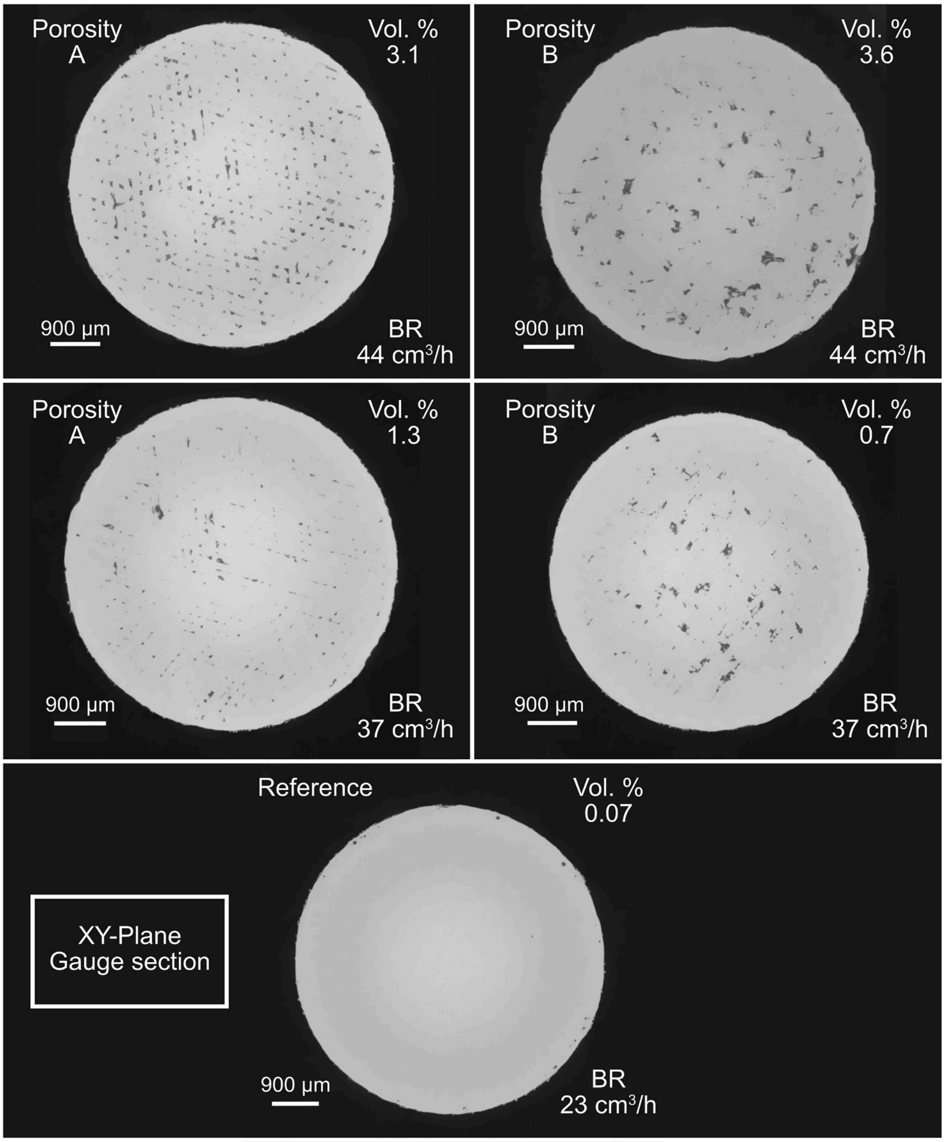

Fig. 2. XCT cross-sections of the gauge region (XY-plane) showing the distribution and pore size of different as-built conditions processed at varying build rates (BR), along with the measured porosity volume fraction (Vol. %).

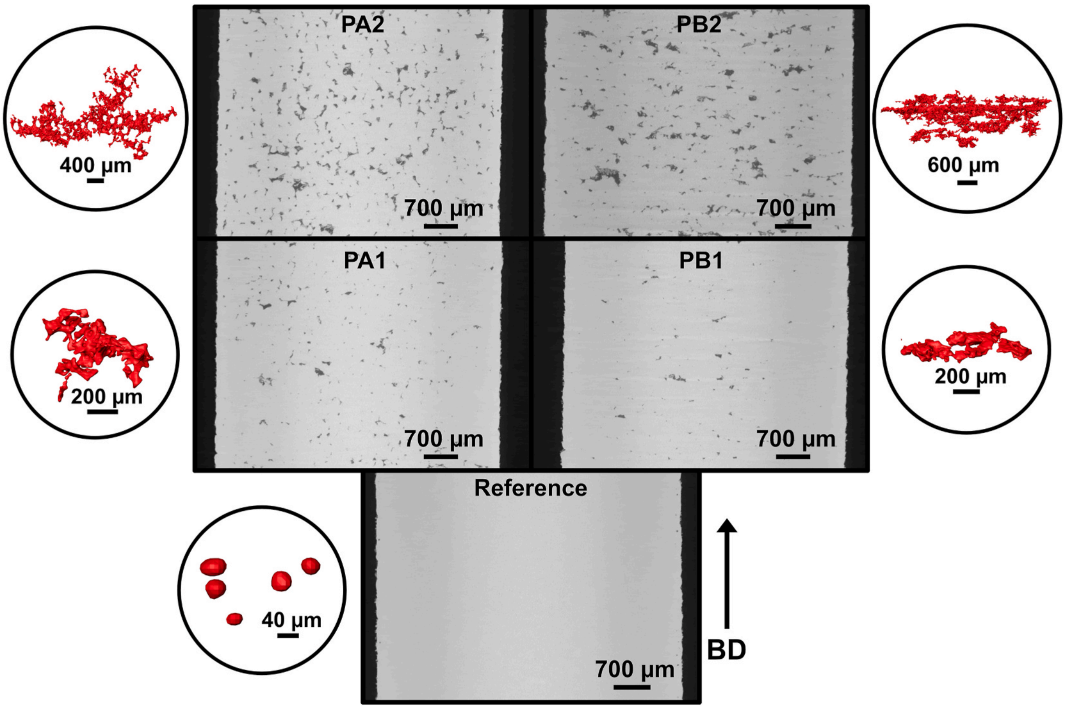

Fig. 3. XCT visualization of the porosity distribution along the build direction for different as-built conditions, accompanied by the largest pores highlighted in red.

Figs. 4 and 5 present a quantitative analysis of pore characteristics focusing on size, distribution, shape, and orientation angle relative to the build direction for the different as-built conditions. With increasing build rate, larger pores occupy a greater proportion of the total pore area. As shown in Fig. 4a and b, the cumulative area fraction curves shift toward higher equivalent diameters, indicating that defects grow both in size and in their contribution to the overall pore fraction. The PB conditions show broader distributions with a greater number of large pores. For the PB2 condition, even at 200 μm, the cumulative area fraction is still relatively low (approximately 0.4), indicating the presence of numerous larger pores, whereas in the reference condition, nearly all pore area is accounted by pores below 100 μm. This demonstrates that increased scan speed has a stronger influence on pore size than hatch spacing at the same build rate.

The evolution of pore shape and orientation is summarized in Fig. 5a and b. As build rate increases, a reduction in sphericity is observed, specifically in the high build rate conditions, reflecting a shift from rounded gas pores to more irregular, LoF type porosity. It is seen that the reference condition (Fig. 5a) maintains the highest sphericity values, with no pores below 0.6 sphericity. This is consistent with the presence of small, nearly spherical gas pores captured by XCT (Fig. 3). At an intermediate build rate, PA1 and PB1 display nearly identical cumulative trends in sphericity, suggesting that both increased hatch spacing and scan speed introduce similar levels of shape irregularity. However, at the highest build rates, PB2 shows a pronounced reduction in sphericity compared to PA2, indicating larger irregularity likely linked to unstable melt pool behaviour and the formation of inter-layer LoF pores [25,26].

Regarding pore orientation (Fig. 5b), the interpretation of the reference condition is limited, as the pores are small and nearly spherical, making their orientation difficult to define. Among the process modified conditions, PB1 and PB2 exhibit similar overall orientation profiles, with most pores oriented at small angles, indicating a directional preference perpendicular to the build direction. This suggests that increased scan speed in PB conditions promotes inter-layer LoF pores that preferentially form within the plane between layers. For increased hatch distances the PA conditions show incremental shifts toward higher

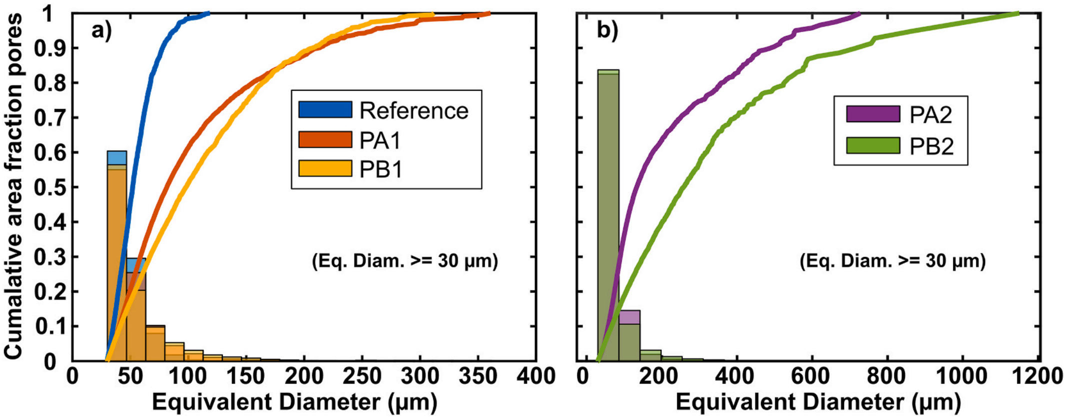

Fig. 4. Statistical analysis of pore characteristics for different as-built conditions: a) cumulative area fraction and size distribution of pores with equivalent diameter ≥30 μm for the reference, PA1, and PB1 conditions. Further, in b) the same analysis for PA2 and PB2 at higher build rates with an extended x-axis to reflect larger pore sizes.

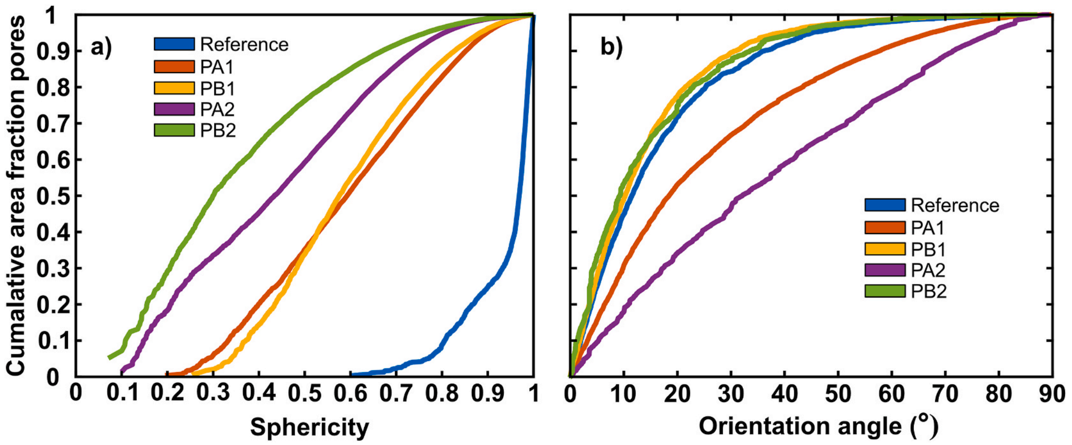

Fig. 5. Statistical analysis of pore characteristics for different as-built conditions: a) cumulative area fraction of pores as a function of sphericity, and b) cumulative area fraction as a function of orientation angle relative to the build direction (0° = perpendicular, 90° = parallel).

orientation angles with increasing build rate, as indicated by the reduced slope at lower angles. This trend suggests a tendency for pores to align more parallel to the build direction, although this is difficult to capture due to the interconnected nature of pores observed in XCT reconstructions (Fig. 3).

These observations imply that while PB conditions promote horizontally aligned inter-layer LoF driven by high scan speeds, PA conditions tend to result in more vertically oriented inter-hatch LoF pores with similar distribution and pore morphologies as build rate increases.

3.3. *Influence of build rate and surface finishing on fatigue life*

The results of fatigue testing are presented in the S–N plot in Fig. 6, showing the number of cycles to failure (Nf) as a function of stress amplitude (100–275 MPa) in logarithmic scale for all as-built and surface-treated samples. Linear regression fits were applied according to the Basquin relation to evaluate the fatigue strength exponent (*b*) for each condition [27,28].

The reference condition, corresponding to the lowest build rate, exhibits the longest fatigue life among the as-built specimens, highlighting the importance of minimizing internal defects to enhance fatigue performance [2]. When comparing PA and PB conditions, the PA samples demonstrate longer and more consistent fatigue lives at comparable build rates and stress levels. A gradual reduction in fatigue performance is observed from PA1 to PA2, corresponding to the increase in pore fraction and size. In contrast, PB1 and PB2 show not only shorter fatigue lives but also more scatter, which correlates with the presence of more detrimental pore features i.e. larger, sharper and randomly distributed defects and a higher fraction of open porosity as identified through XCT analysis (Figs. 3–5). Notably, despite PA1 having a higher pore fraction (1.3%) than PB1 (0.7%), it still exhibits longer fatigue life and lower scatter, emphasizing that pore morphology, orientation, and surface connectivity are more influential for fatigue performance than total pore content alone [9].

The Basquin exponents (Fig. 6) further support this trend. The reference and surface-treated samples show steeper slopes (b ≈ −0.35), while the PB conditions exhibit flatter slopes (PB1: −0.182, PB2: −0.138). Such flattening is indicative of a defect-controlled regime where fatigue life is governed by the largest flaw, consistent with the increased scatter and broader defect size distribution observed in the PB samples [29,30].

Furthermore, the orientation of pores in PB conditions, with a greater proportion aligned perpendicular to the build and loading direction, likely intensifies fatigue degradation by presenting a larger effective defect area under stress. This could explain the lower fatigue performance of PB conditions, despite the similar surface roughness values measured across all as-built samples (Table 3). These results indicate that pore characteristics, specifically size, morphology, distribution, and orientation are the primary factors governing fatigue life in the as-built state, with a stronger influence than surface roughness.

Although variations in volumetric energy density (VED) can alter melt pool geometry and influence microstructural features such as grain morphology and residual stress state [1], the relative importance of these factors depends on the defect population. In near-fully dense

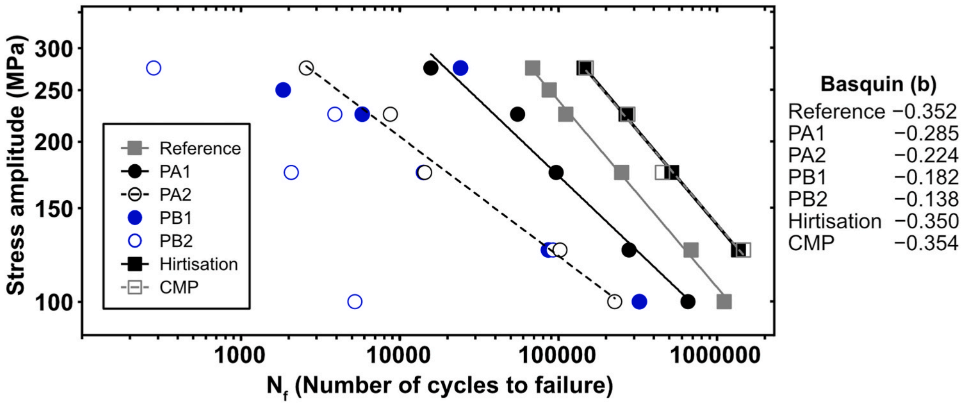

Fig. 6. (S–N) curves for the as-built conditions produced at three different build rates, categorized into two porosity types (A and B), alongside surface-treated reference samples (Hirtisation® and CMP). The x-axis gives the number of cycles to failure (N_f) and the y-axis shows the stress amplitude (MPa) both on a logarithmic scale.

material, variations in melt pool geometry and associated microstructural characteristics may influence fatigue crack initiation and propagation. However, in the present study, increased build rates intentionally introduced porosity levels up to several percent (1-5%), including LoF defects exceeding 100 μm in size [3]. In the high-cycle fatigue regime, such defects act as dominant stress concentrators that govern crack initiation. Previous studies on PBF-LB 316L have shown that when significant internal or surface-connected pores are present, fatigue performance is primarily controlled by defect size, morphology, and position rather than by microstructural variations [2,12,31]. Therefore, within the parameter space investigated here, porosity is considered the primary driving factor controlling fatigue life.

Surface treatments applied to the reference condition, namely Hirtisation® and CMP, lead to a marked improvement in fatigue performance, approximately doubling the fatigue life compared to the untreated reference. This emphasizes the critical role of surface integrity in fatigue resistance, particularly through the elimination or mitigation of surface roughness. It should be noted that these surface treatments were applied only to reference condition samples, their potential benefits for PA and PB conditions remain to be considered.

3.4. Fractography

Fractography analysis of the tested samples was carried out to investigate fatigue failure mechanisms across different build rates and surface conditions. The reference sample (Fig. 7a) shows a relatively smooth fracture surface with multiple surface initiation sites, as indicated by the arrows, and a slanted region at the bottom, characteristic of final ductile failure. A higher magnification image of the surface edge (Fig. 7b) reveals a surface valley, approximately 100 μm deep, which aligns with the surface roughness measurements. The local morphology, including the gently curved boundary and radiating river-like features, suggests that this valley acted as a crack initiation site.

3.4.1. Influence of hatch distance (porosity type A)

In contrast to the reference condition, PA1 (Fig. 8a and b), produced using an increased hatch distance, exhibits a more irregular fracture surface. The overview (Fig. 8a) shows a lack of a clearly defined crack front, suggesting multiple initiation sites and complex crack paths. The magnified region (Fig. 8b) reveals a rougher fracture morphology, where partially fused powder particles and inter-hatch LoF pores can be seen. These features likely acted as distributed crack initiation sites, promoting crack propagation along these planes [31]. The presence of a deep, irregular central region further suggests that the crack advanced across several build layers proving the complex interconnected network of pores.

With a further increase in hatch distance, the fracture surface of PA2 (Fig. 8c and d) becomes even more irregular. The overview (Fig. 8c) shows extensive multiple interconnected fracture paths. At higher magnification (Fig. 8d), a dense network of interconnected LoF pores is visible, extending not only between hatch lines but also between layers. In PA2, higher fraction of unfused powder is observed both within the pore network and on the top surfaces of fractured melt pools, providing clear evidence of incomplete fusion across both scanning directions. These features collectively indicate that increased hatch distance facilitates multi crack initiation and crack propagation through an interconnected LoF pore network, significantly reducing fatigue resistance.

3.4.2. Influence of scan speed (porosity type B)

Locating the exact crack initiation site for PB1 is somewhat challenging due to the presence of multiple surface-connected features. The overview image (Fig. 9a) shows a relatively smooth fracture surface, with some irregularities suggesting delamination-like failure along internal planes. The magnified region (Fig. 9b) reveals a pronounced surface valley, directly connected to subsurface LoF pores. This suggests that fatigue crack initiation was influenced by the combination of surface roughness and inter-layer LoF defects, which likely acted together to promote multi-site initiation and rapid crack propagation and accelerated failure.

At the highest build rate (PB2), the fracture surface (Fig. 9c) appears significantly more irregular than that of PB1, with extensive crack branching. Large LoF pores are visible even at low magnification, including a prominent crater-like feature indicated by the black arrow. The higher magnification view (Fig. 9d) reveals surface-connected pores linked to subsurface internal LoF defects, supporting the interpretation that crack initiation and propagation were dominated by inter-layer LoF pores, specifically those connected to the surface.

A direct comparison between PA1 and PB1 highlights the importance of defect morphology over pore fraction. Although PA1 exhibits a higher pore fraction than PB1, it shows longer fatigue life and more consistent fracture behaviour. Fractography of PA1 revealed inter-hatch LoF porosity, which promoted crack propagation along predictable paths between hatch melt tracks. In contrast, PB1 displayed inter-layer LoF porosity, often resembling delamination, with irregular, surface-connected defects that facilitate earlier crack initiation and rapid crack propagation and hence lead to greater scatter in fatigue life. These observations reinforce that defect size, geometry, and surface connectivity are the primary factors driving scatter in fatigue life and play a more critical role at high build rates than overall pore content.

3.4.3. Post AM surface treatment

Fig. 10 shows SEM micrographs of fracture surfaces from the

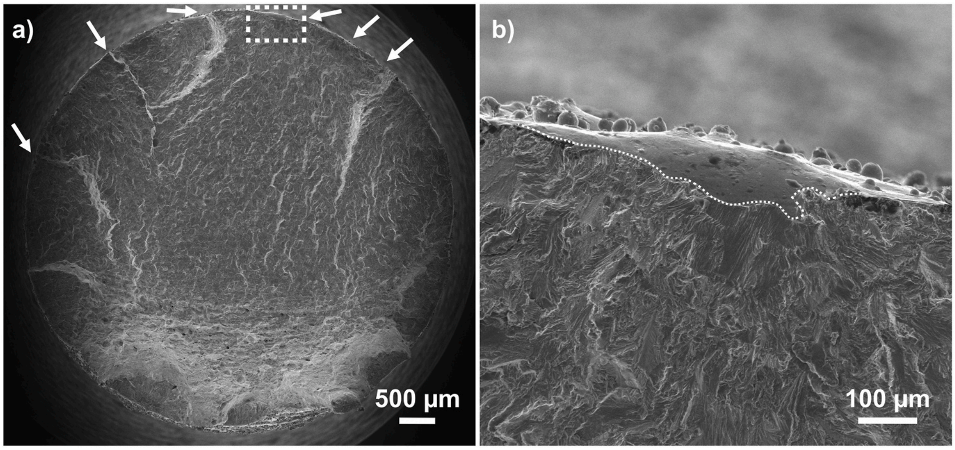

Fig. 7. Fracture surface of reference condition fatigue sample showing a) low magnification overview illustrating multiple crack initiation sites along the sample edge (indicated by arrows). In b) higher magnification shows a typical initiation site with a surface notch or irregularity (>100 μm).

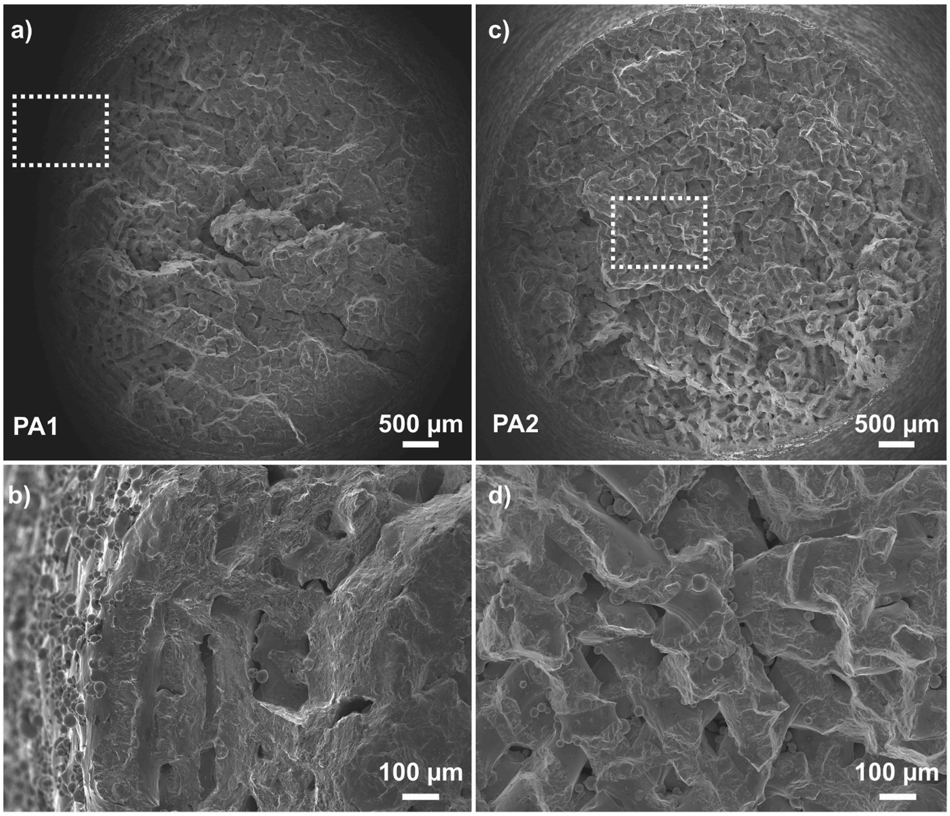

Fig. 8. SEM micrographs of fracture surfaces for porosity type A, showing a) and c) overview images and b) and d) higher magnification views of potential cracks path regions for PA1 and PA2, respectively.

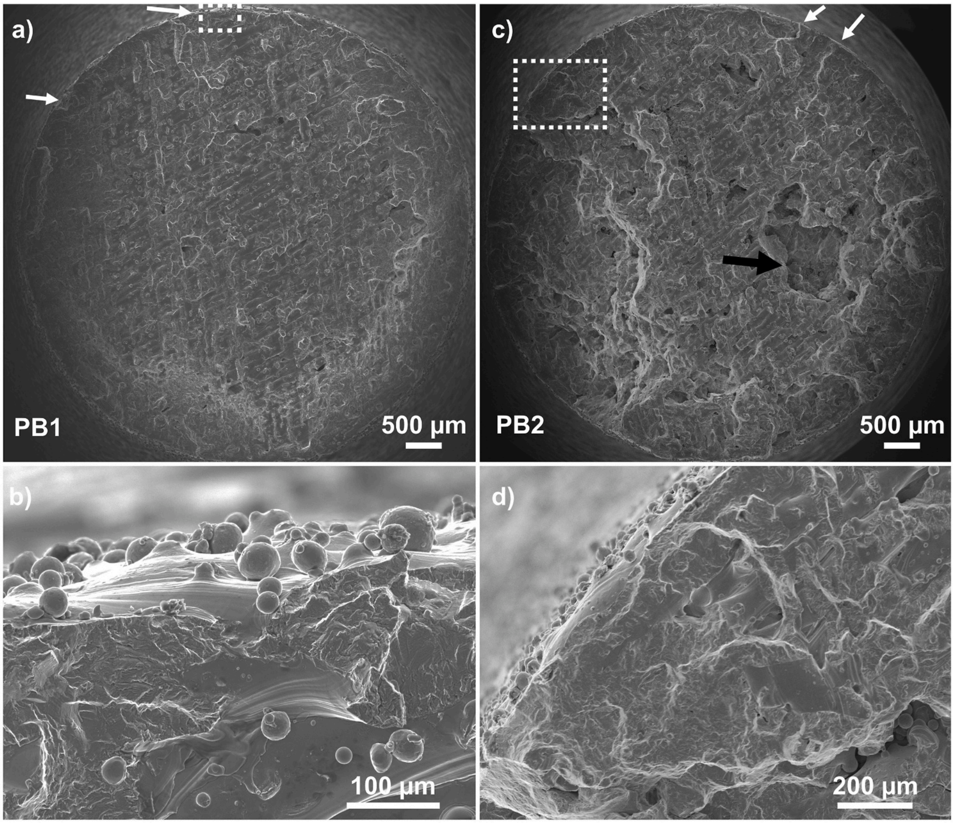

Fig. 9. SEM micrographs of fracture surfaces for porosity type B, showing overview (a, c) and magnified regions (b, d) for PB1 and PB2 conditions, revealing potential crack initiation sites and propagation paths influenced by surface valleys and LoF pores.

reference samples after surface treatment by CMP (Fig. 10a and b) and Hirtisation® (Fig. 10c and d). As indicated by the S–N curves (Fig. 6), both treatments significantly improved fatigue life compared to the as-built condition.

The CMP-treated specimen (Fig. 10a) displays a relatively smooth fracture surface. However, higher magnification (Fig. 10b) reveals distinct crack initiation sites, each associated with semi-spherical surface features as previously shown in (Fig. 1c). CMP involved targeted material removal of approximately 110 μm, a depth chosen to preserve the contour layer and avoid exposing larger subsurface pores observed in higher build-rate conditions. For the reference condition, XCT (Fig. 2) results indicated the presence of spherical pores in the contour/bulk overlap zone. These pores were likely exposed by the CMP process, as suggested by the semi-spherical surface features seen in Fig. 10b and subsequently acted as crack initiation sites during fatigue loading. These observations suggest that removing at least an additional 100 μm may have eliminated such defects and further improved fatigue performance, considering that *S10z* for the as-built specimen was (150 ± 20) μm.

In contrast, no clear crack initiation site could be identified on the fracture surface of the Hirtisation®-treated sample (Fig. 10c). The overall fracture surface shows a fibrous slant region near the bottom, indicative of final failure. Previous studies have shown that Hirtisation® preferentially removes material at melt pool boundaries, potentially forming shallow notch-like features [18]. However, no fracture features in this sample suggest that crack initiation occurred at these etched boundaries. Despite altering the surface morphology, Hirtisation® appears to have effectively removed subsurface defects. Notably, a greater material removal depth of approximately 400 μm was applied in this case, which contributed to the suppression of subsurface pores.

Despite the differences in material removal depth, both CMP and Hirtisation® resulted in similar improvements in fatigue life (Fig. 7). This is notable considering that Hirtisation® removed a greater amount of material (~400 μm), likely eliminating subsurface pores at the contour/bulk interface, while CMP (~110 μm) left behind semi-spherical surface features (Fig. 10b). The comparable fatigue performance between CMP and Hirtisation® suggests that, although CMP exposed features that may serve as initiation sites, their detrimental effect may be mitigated by the compressive residual stress induced by the mechanical-media interaction process [16]. Whereas the residual stresses near the surface of samples processed by Hirtisation have measured tensile stresses near the yield limit of the material [23]. A detailed investigation of both parameters is essential in future studies to fully understand their role in fatigue resistance following surface treatment.

4. Conclusions

The influence of pore characteristics, surface roughness and surface treatment at increased build rates on the HCF fatigue life of PBF-LB 316L stainless steel were studied. Based on the findings of this work the following conclusions can be made.

- Increasing the build rate, through both increased hatch distance (PA) and increased scan speed (PB), resulted in a significant reduction in high-cycle fatigue (HCF) life compared to the reference condition produced at the lowest build rate.

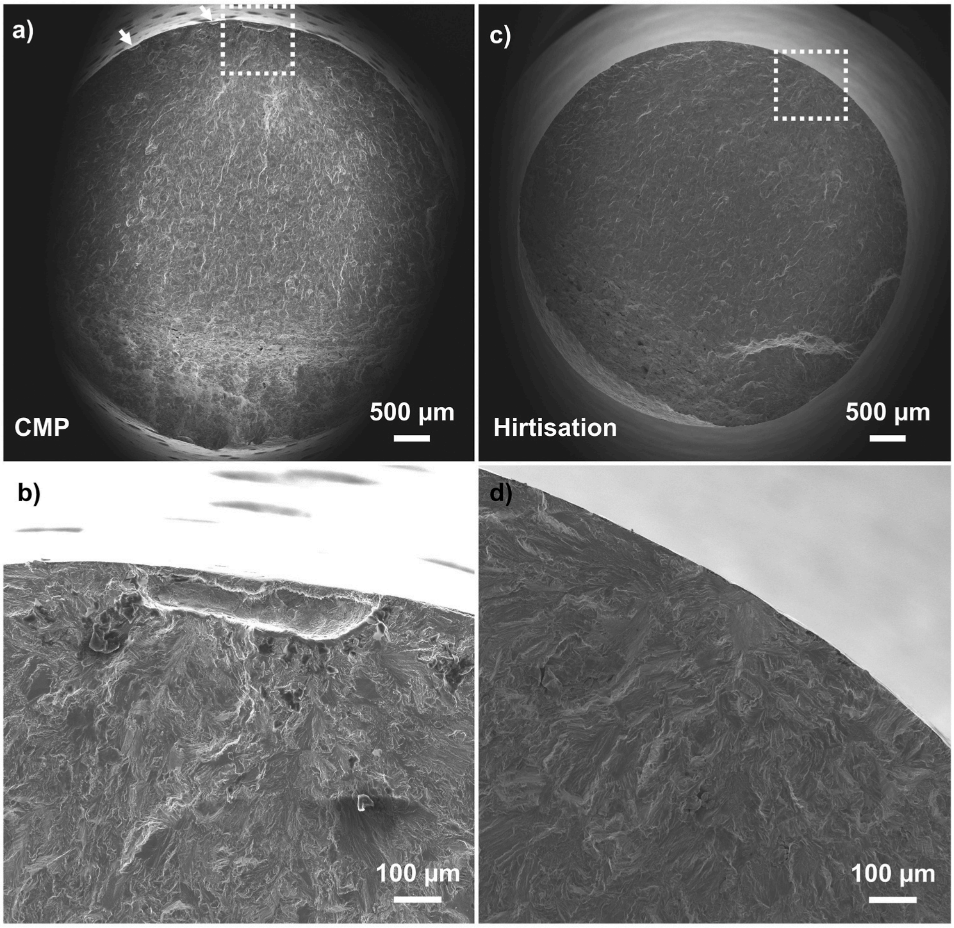

Fig. 10. SEM micrographs of fracture surfaces for surface-treated reference samples: (a, b) CMP-treated sample showing potential initiation sites at surface cracks with cellular structures, and (c, d) Hirtisation® treated sample showing melt pool boundaries without clear surface-initiated cracks.

- The strategy used to increase the build rate significantly affected the morphology and distribution of porosity, which in turn had a dominant effect on fatigue performance.
- Increased hatch distance (PA) led to a more uniform distribution of interconnected LoF pores along hatch lines, resulting in a low scatter in fatigue life.
- Increased scan speed (PB) produced larger, more randomly distributed LoF pores, many of which were surface-connected and preferentially oriented perpendicular to the loading direction. These characteristics contributed to shorter and more scattered fatigue life.
- While all as-built conditions exhibited significant surface roughness, the statistical analysis showed no significant difference between them. This suggests that internal pore characteristics were the primary drivers of fatigue life in the as-built state.
- Both Chemical Mechanical Polishing (CMP) and Hirtisation® surface treatments substantially enhanced the HCF fatigue life of as-built reference condition, providing an approximate doubling of fatigue life.
- Hirtisation® removed subsurface pores due to more material removal (~400 μm), while CMP (~110 μm) opened surface-connected features. Nonetheless, both treatments yielded similar fatigue performance, suggesting that partial defect mitigation and changes in surface condition or residual stress can meaningfully delay crack initiation.

The present findings indicate that increased build rates, although associated with reduced as-built fatigue performance, may represent a viable manufacturing strategy when combined with appropriate surface treatments and process parameters. Since higher build rates reduce machine time and associated capital cost per component, a trade-off emerges between productivity and post-processing effort. For components where surface treatments can be efficiently applied, producing parts at elevated build rates followed by surface finishing may provide a competitive alternative to low build rate processing aimed at near-full density in the as-built condition.

Declaration of competing interest

The authors declare that they have no known competing financial interests or personal relationships that could have appeared to influence the work reported in this paper.

Acknowledgement

This work was performed in the frame of the Centre for Additive Manufacture - Metal (CAM^2), [Dnr: 2022-03076] supported by the Swedish Agency for Innovation Systems Vinnova.

References

[1] DebRoy T, Wei HL, Zuback JS, Mukherjee T, Elmer JW, Milewski JO, Beese AM, Wilson-Heid A, De A, Zhang W. Additive manufacturing of metallic components – process, structure and properties. Prog Mater Sci 2018;92:112–224. https://doi.org/10.1016/j.pmatsci.2017.10.001.

[2] Liang X, Hor A, Robert C, Salem M, Lin F, Morel F. High cycle fatigue behavior of 316L steel fabricated by laser powder bed fusion: effects of surface defect and loading mode. Int J Fatigue 2022;160:106843. https://doi.org/10.1016/j.ijfatigue.2022.106843.

[3] Andreau O, Pessard E, Koutiri I, Peyre P, Saintier N. Influence of the position and size of various deterministic defects on the high cycle fatigue resistance of a 316L steel manufactured by laser powder bed fusion. Int J Fatigue 2021;143:105930. https://doi.org/10.1016/j.ijfatigue.2020.105930.

[4] Gockel J, Sheridan L, Koerper B, Whip B. The influence of additive manufacturing processing parameters on surface roughness and fatigue life. Int J Fatigue 2019;124:380–8. https://doi.org/10.1016/j.ijfatigue.2019.03.025.

[5] Taghian M, Hossein M, Lannunziata E, Del G, Iuliano L, Saboori A. Laser powder bed fusion of metallic components : latest progress in productivity , quality , and cost perspectives. J Mater Res Technol 2023;27:6484–500. https://doi.org/10.1016/j.jmrt.2023.11.049.

[6] Pfalz T, Rota A, Saeidnezhad N, Leyens C. Comparison of different multi-laser powder bed fusion exposure strategies and their influence on the part quality of IN718. Int J Adv Manuf Technol 2023;128:4469–90. https://doi.org/10.1007/s00170-023-12194-3.

[7] Kose H, Jin M, Peng T. Quality and productivity trade-off in powder-bed additive manufacturing. Progr Addit Manuf 2020;5:199–210. https://doi.org/10.1007/s40964-020-00122-w.

[8] Schwerz C, Schulz F, Natesan E, Nyborg L. Increasing productivity of laser powder bed fusion manufactured Hastelloy X through modification of process parameters. J Manuf Process 2022;78:231–41. https://doi.org/10.1016/j.jmapro.2022.04.013.

[9] Gong H, Rafi K, Gu H, Janaki Ram GD, Starr T, Stucker B. Influence of defects on mechanical properties of Ti-6Al-4V components produced by selective laser melting and electron beam melting. Mater Des 2015;86:545–54. https://doi.org/10.1016/j.matdes.2015.07.147.

[10] Du C, Zhao Y, Jiang J, Wang Q, Wang H, Li N, Sun J. Pore defects in Laser Powder Bed Fusion: formation mechanism, control method, and perspectives. J Alloys Compd 2023;944:169215. https://doi.org/10.1016/j.jallcom.2023.169215.

[11] Leicht A, Fischer M, Klement U, Nyborg L, Hryha E. Increasing the productivity of laser powder bed fusion for stainless steel 316L through increased layer thickness. J Mater Eng Perform 2021;30:575–84. https://doi.org/10.1007/s11665-020-05334-3.

[12] Choo H, White LP, Xiao X, Sluss CC, Morin D, Garlea E. Deformation and fracture behavior of a laser powder bed fusion processed stainless steel: in situ synchrotron x-ray computed microtomography study. Addit Manuf 2021;40:101914. https://doi.org/10.1016/j.addma.2021.101914.

[13] Kim WY, Yoon EY, Kim JH, Kim S. Surface characteristics of Ti–6Al–4V alloy based on the process parameter and abrasive process in the laser powder bed fusion. Met Mater Int 2023;29:2345–57. https://doi.org/10.1007/s12540-022-01378-3.

[14] Glaubitz EB, Fox JC, Kafka OL, Gockel J. Contour parameters, melt pool behavior, and surface roughness relationships across laser powder bed fusion platforms and metallic alloys. Int J Adv Manuf Technol 2025:4419–37. https://doi.org/10.1007/s00170-025-15066-0.

[15] SIS (Swedish Standards Institute). Svensk Standard, Ss 812310:2014. 24, www.sis.se; 2018.

[16] Gunnerek R, Soundarapandiyan G, Mishurova T, Schröder J, Bruno G, Boykin J, Diaz A, Klement U, Hryha E. Chemical mechanical polishing of powder bed fusion – laser beam processed 316 L stainless steel. J Mater Process Technol 2025:119055. https://doi.org/10.1016/j.jmatprotec.2025.119055.

[17] Hirtisation surface treatment of printed metal | RENA. n.d. https://www.rena.com/en/technology/process-technology/hirtisation. [Accessed 30 August 2024].

[18] Gunnerek R, Soundarapandiyan G, Christoph M, Hryha E, Klement U. Transactions of the IMF the International Journal of Surface Engineering and Coatings Influence of microstructure and surface topography on material removal by the Hirtisation ® process. Transactions of the IMF 0 2024:1–8. https://doi.org/10.1080/00202967.2024.2411903.

[19] SIS (Swedish Standards Institute). Metalliska material-utmattningsprovning-metod med axial kraftkontroll. 36, www.sis.se; 2018.

[20] Practice for statistical analysis of Linear or linearized stress-life (S-N) and strain-life (-N) fatigue data. https://doi.org/10.1520/E0739-10R15; 2015.

[21] Snyder JC, Thole KA. Understanding Laser powder bed fusion surface roughness. J Manuf Sci Eng 2020;142. https://doi.org/10.1115/1.4046504.

[22] Risposi T, Rusnati L, Patriarca L, Hardaker A, Luczyniec D, Beretta S. Fatigue of Ti6Al4V manufactured by PBF-LB: a comparison of failure mechanisms between net-shape and electro-chemically milled surface conditions. Eng Fail Anal 2025;172:109403. https://doi.org/10.1016/j.engfailanal.2025.109403.

[23] Manchili SK, Pezzotti F, Dartfeldt E, Halmdienst M, Klement U, Hosseini S. Chemical and electrochemical surface modification and fatigue response of PBF-LB/M 316L stainless steel. Progr Addit Manuf 2026. https://doi.org/10.1007/s40964-025-01482-x.

[24] Lindström SB, Moverare J, Franke M, Persson J, Leidermark D, Thore CJ, Lindström T, Kapidžić Z. Fatigue life prediction for PBF-LB Ti6A14V with as-built surface under nonproportional loads using an incremental fatigue damage model. Int J Fatigue 2025;193:108777. https://doi.org/10.1016/j.ijfatigue.2024.108777.

[25] Schwerz C, Nyborg L. Linking in situ melt pool monitoring to melt pool size distributions and internal flaws in laser powder bed fusion. Metals 2021;11. https://doi.org/10.3390/met11111856.

[26] Young ZA, Guo Q, Parab ND, Zhao C, Qu M, Escano LI, Fezzaa K, Everhart W, Sun T, Chen L. Types of spatter and their features and formation mechanisms in laser powder bed fusion additive manufacturing process. Addit Manuf 2020;36:101438. https://doi.org/10.1016/j.addma.2020.101438.

[27] Werner T, Madia M, Zerbst U. Comparison of the fatigue behavior of wrought and additively manufactured AISI 316L. In: Procedia structural integrity. Elsevier B.V.; 2021. p. 554–63. https://doi.org/10.1016/j.prostr.2022.03.056.

[28] Stern F, Becker L, Cui C, Tenkamp J, Uhlenwinkel V, Steinbacher M, Boes J, Lentz J, Fechte-Heinen R, Weber S, Walther F. Improving the defect tolerance of PBF-LB/M processed 316L steel by increasing the nitrogen content. Adv Eng Mater 2023;25. https://doi.org/10.1002/adem.202200751.

[29] Murakami Y, Takagi T, Wada K, Matsunaga H. Essential structure of S-N curve: prediction of fatigue life and fatigue limit of defective materials and nature of scatter. Int J Fatigue 2021;146. https://doi.org/10.1016/j.ijfatigue.2020.106138.

[30] Niu X, Zhu SP, He JC, Liao D, Correia JAFO, Berto F, Wang Q. Defect tolerant fatigue assessment of AM materials: size effect and probabilistic prospects. Int J Fatigue 2022;160. https://doi.org/10.1016/j.ijfatigue.2022.106884.

[31] Andreou O, Pessard E, Koutiri I, Penot JD, Dupuy C, Saintier N, Peyre P. A competition between the contour and hatching zones on the high cycle fatigue behaviour of a 316L stainless steel: analyzed using X-ray computed tomography. Mater Sci Eng, A 2019;757:146–59. https://doi.org/10.1016/j.msea.2019.04.101.